ACS central science

http://pubs.acs.org/journal/acscii

Research Article

Cryo-EM, Protein Engineering, and Simulation Enable the Development of Peptide Therapeutics against Acute Myeloid Leukemia

Kaiming Zhang,*,# Naoki Horikoshi,# Shanshan Li, Alexander S. Powers, Mikhail A. Hameedi, Grigore D. Pintilie, Hee-Don Chae, Yousuf A. Khan, Carl-Mikael Suomivuori, Ron O. Dror, Kathleen M. Sakamoto,* Wah Chiu,* and Soichi Wakatsuki*

Cite This: *ACS Cent. Sci.* 2022, 8, 214–222

Read Online

ACCESS | Metrics & More | Article Recommendations | Supporting Information

ABSTRACT: Cryogenic electron microscopy (cryo-EM) has emerged as a viable structural tool for molecular therapeutics development against human diseases. However, it remains a challenge to determine structures of proteins that are flexible and smaller than 30 kDa. The 11 kDa KIX domain of CREB-binding protein (CBP), a potential therapeutic target for acute myeloid leukemia and other cancers, is a protein which has defied structure-based inhibitor design. Here, we develop an experimental approach to overcome the size limitation by engineering a protein double-shell to sandwich the KIX domain between apoferritin as the inner shell and maltose-binding protein as the outer shell. To assist homogeneous orientations of the target, disulfide bonds are introduced at the target−apoferritin interface, resulting in a cryo-EM structure at 2.6 Å resolution. We used molecular dynamics simulations to design peptides that block the interaction of the KIX domain of CBP with the intrinsically disordered pKID domain of CREB. The double-shell design allows for fluorescence polarization assays confirming the binding between the KIX domain in the double-shell and these interacting peptides. Further cryo-EM analysis reveals a helix−helix interaction between a single KIX helix and the best peptide, providing a possible strategy for developments of next-generation inhibitors.

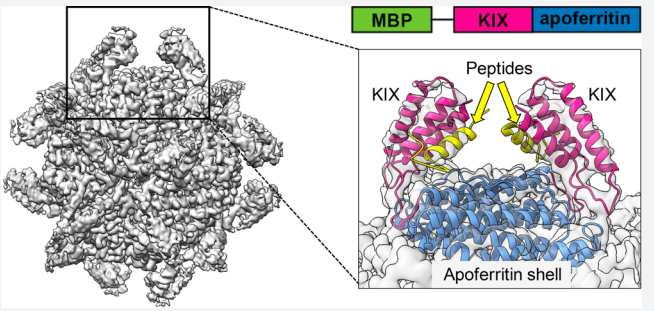

INTRODUCTION

Recent technological breakthroughs in single-particle cryogenic electron microscopy (cryo-EM) have achieved numerous high-resolution structures of macromolecules. For specimens smaller than 40 kDa that cannot be crystallized or imaged by nuclear magnetic resonance (NMR), cryo-EM is also difficult to apply, leading to a big gap in the field of structural biology. Extensive efforts have been made to visualize small proteins, including optimization of sample preparation,[1] application of a phase plate,[2,3] and the design of nanocage systems that link the small proteins to larger molecules with a known structure.[4−7] However, the molecular weight of the smallest protein determined by cryo-EM at better than 3.5 Å resolution is still higher than 50 kDa.[3] Besides proteins, some small RNAs less than 50 kDa have been studied by cryo-EM, achieving a 3.7 Å resolution structure for a 40 kDa SAM-IV riboswitch.[8] However, to date, no polypeptides below 40 kDa have been resolved to better than 4 Å by single-particle cryo-EM. This study demonstrates that the fusion of small proteins to a cage-like structure is a feasible solution to break the resolution limit for cryo-EM structural determination of small biomolecules.

RESULTS AND DISCUSSION

Here, we design a double-shell system, cross-linked with disulfide bonds, to the 11 kDa KIX domain of CREB-binding protein (CBP), which interacts with a number of transcription factors implicated in cancer progression including the progression of acute myeloid leukemia (AML).[9−11] For example, poor prognosis in AML is associated with the protein−protein interaction between the phosphorylated KID (pKID) domain of Cyclic AMP Response Element Binding protein (CREB) and the KIX domain (11 kDa) of its interaction partner CREB-binding protein (CBP). The KIX−pKID interaction has been the target of inhibitor design for therapeutics against AML, but its progress has been hampered by the lack of high-throughput structure determination of the complex due to the intrinsically flexible nature of both

Received: September 8, 2021
Published: February 7, 2022

domains. The double-shell system uses the apoferritin as the inner cage because of its high rigidity, symmetry, and easily achievable atomic resolution cryo-EM structure.[12] The KIX domain of CBP is genetically engineered to fuse directly to the N-terminus of apoferritin, and the maltose-binding protein (MBP) is fused to the N-terminus of the KIX domain to facilitate its purification (Figure 1a). We expect that the MBP is located at the most exterior part of the complex and thus may protect and/or rigidify the small protein of interest, namely, the KIX domain.

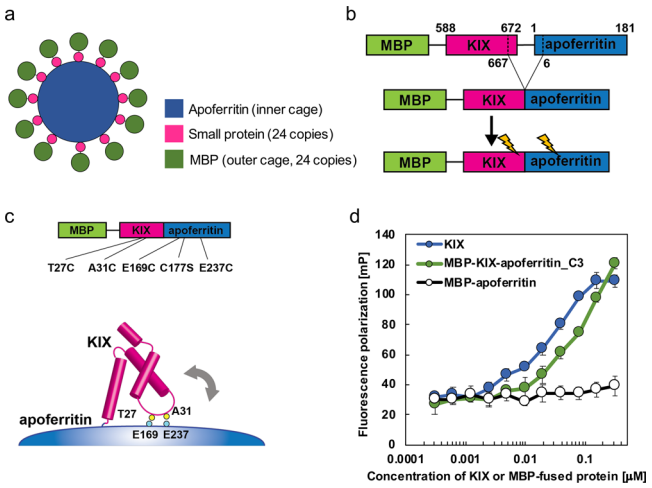

Figure 1. Design of the double-shell system. a. The double-shell system is shown by cartoon with apoferritin as inner cage, MBP as outer cage, and small cargo proteins in the middle portion. b. Strategy of plasmid construction. The cargo protein KIX C-terminus is fused to the apoferritin N-terminus with the C-terminal 668−672 residues of KIX and N-terminal 1−5 residues of apoferritin truncated for stability. Several mutations (shown as lightning) were also incorporated on the interface between KIX and apoferritin to enhance stability. The MBP tag is fused to the KIX N-terminus. c. Design of mutations that stabilize the KIX domain of CBP on the apoferritin complex. Diagram of the protein construct with mutations (top). Three-dimensional arrangement of the KIX domain of CBP on the apoferritin complex (bottom). The positions of the five residues that were mutated to cysteine or serine were shown. d. Fluorescence polarization assay using the BODIPY-conjugated phosphorylated KID domain ($pKID^{BODIPY}$) of CREB and KIX, MBP-KIX-apoferritin construct 3, or MBP-apoferritin. KIX, MBP-KIX-apoferritin construct 3, or MBP-apoferritin were titrated into a solution of 200 nM $pKID^{BODIPY}$.

The CBP KIX domain is known to be flexible,[13] defying high-resolution X-ray structural analysis. Indeed, for a long time, the only known structures of the KIX domain were determined by NMR, until the work by Wang and colleagues[14] who conjugated a small compound to stabilize the KIX helices. Unfortunately, the putative pKID domain-binding site of the KIX is covered by a neighboring KIX molecule in the crystal, making it impossible to do small compound soaking experiments, needed for the development of inhibitors for the CREB−CBP interaction. We made similar attempts and obtained KIX crystals which diffracted to a high resolution resulting in a similar structure with the same packing issue. Extensive cocrystallization trials of the 1−10 compound-conjugated KIX domain with a number of small molecule compounds were not successful. The cognizant protein domain, pKID, is even more challenging since it is intrinsically disordered. These issues have hindered structure-based protein−protein interaction inhibitor design. In contrast, the cryo-EM single-particle analysis does not rely on the availability of high-quality crystals, and there is no need to worry about the crystal contacts which might force proteins in certain conformational states. However, the molecular weight of the KIX domain is only ∼11 kDa, way smaller than the current threshold for high-resolution protein structure determination using cryo-EM.[15] Hence, we explore the feasibility of designing a double-shell scaffold for this KIX domain and complex with its inhibitor to make them amenable to single-particle cryo-EM structural determinations.

After examining the structure of the octahedrally arranged, 24-subunit apoferritin (PDB ID: 3WNW), and the NMR and crystal structures of the KIX domain of CBP (PDB IDs: 1KDX and 4I9O), we conceived engineering a chimeric protein by fusing one KIX domain to each of the 24 subunits in the apoferritin, in which the C-terminus (residues: 668−672) of the KIX domain and the N-terminus (residues: 1−5) of apoferritin were truncated to reduce possible flexibility (Figure 1b and Figure S1a). The reason for the C-terminal truncation of the six residues of the KIX domain is because these residues are disordered in the crystal structure (4I9O) and the removal of the six residues does not affect the binding affinity significantly (103.2 nM vs 122.4 nM with the six residue truncation).[16] Therefore, we renumbered the residues of the KIX domain (588−667) and apoferritin (6−181) to 1−80 (KIX) and 81−251 (apoferritin) (Figure S1). In all four constructs used for cryo-EM work in this study, an MBP tag was fused with KIX and apoferritin to facilitate protein purification and possibly reduce the air−water interface-induced damage to the KIX domain and apoferritin cage during the specimen vitrification step (Figure 1b). The initial cryo-EM two-dimensional (2D) analysis of construct 1 and construct 2 of the MBP-KIX-apoferritin revealed that the KIX domain on apoferritin is flexible because of the discontinuous density at the N terminus of the apoferritin, which resides at the exterior surface of the cage (Figure S1c,d). To improve the rigidity of the fused complex, we designed cysteine mutations on the KIX domain and apoferritin to stabilize the KIX domain on apoferritin with disulfide bonds (Figure 1c). By investigating the range of possible orientations of the KIX domain on the apoferritin shell scaffold through direct visualization of the structures, we identified possible residue pairs which can form disulfide bonds (Figure 1c and Figure S1b). In the second design phase, one KIX molecule cross-links with one adjacent apoferritin subunit through two disulfide bonds. The renumbered T27 and A31 residues of the KIX domain and E169/D167 and E237 residues of the apoferritin were mutated to cysteine. In addition, C177 was mutated to serine to prevent the formation of unexpected disulfide bonds. We also deleted a glycine residue between KIX and apoferritin in construct 2 due to its induced subtle flexibility, as demonstrated by worse 2D class averages compared with construct 1, which might interrupt disulfide bonding among T27:E169/D167 and A31:E237. Therefore, we designed additional two constructs (constructs 3 and 4) of the MBP-KIX-apoferritin (Figure S1a,b). The specimens were again screened by cryo-EM 2D analysis, and the protein specimen derived from construct 3 with the best cryo-EM density in the KIX domain was selected for further data collection and processing (Figure 2 and Figure S1e). Hereinafter, we refer to this protein from construct 3 of the

https://doi.org/10.1021/acscentsci.1c01090
ACS Cent. Sci. 2022, 8, 214−222

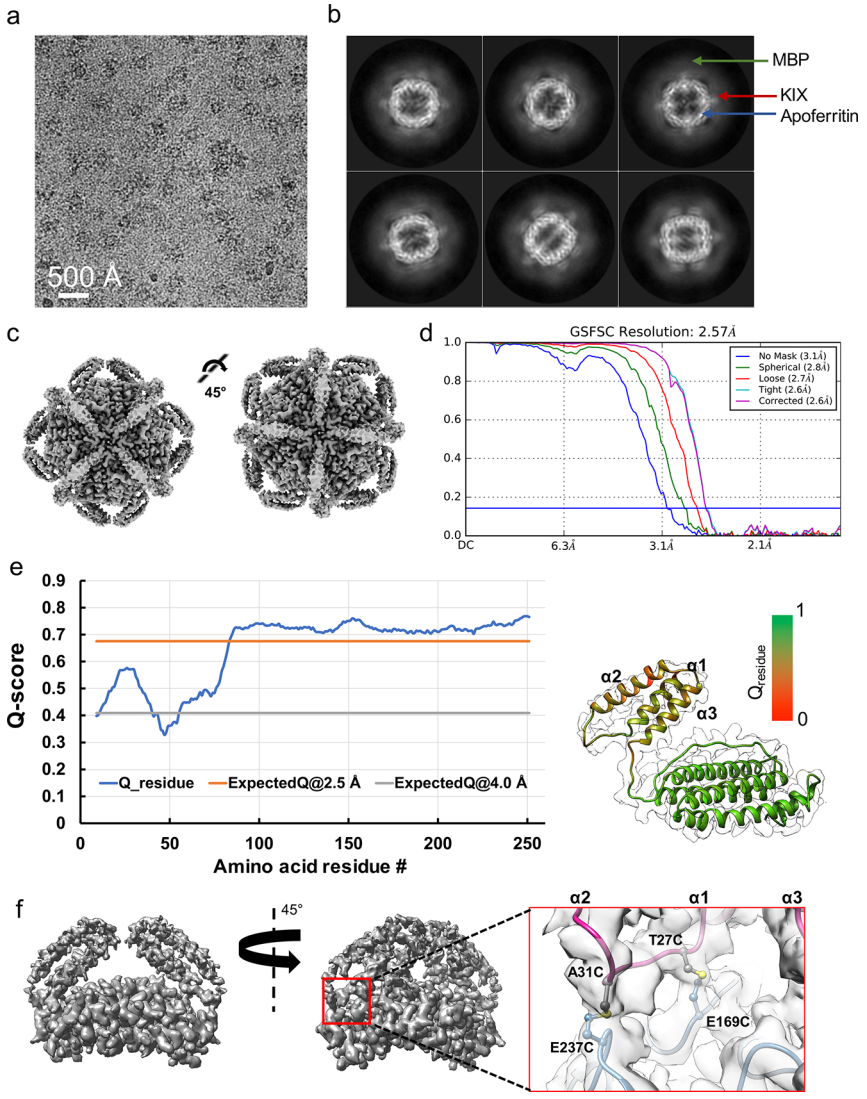

Figure 2. Single-particle cryo-EM analysis of the MBP-KIX-apoferritin complex (MKF). a. Representative motion-corrected cryo-EM micrograph. b. Reference-free 2D class averages (construct 3 in Figure S1). c. Reconstructed cryo-EM map in two different views. d. Gold standard FSC plot for the final 3D reconstruction, calculated in cryoSPARC. e. Q-score for each amino acid residue in model and (2.5−4) Å map of MKF; the orange and gray lines represent the expected Q-scores at 2.5 and 4.0 Å, respectively, based on the correlation between Q-scores and map resolution. Right: The model is shown as ribbon, with residue Q-scores indicated. The higher Q-score indicates better resolvability. f. Left, cryo-EM density of two adjacent subunits in two different views. Right, zoomed view to show the two disulfide bonds between KIX and apoferritin, and the positions of three helices are annotated.

MBP-KIX-apoferritin complex as MKF. The MKF complex was also examined for the binding affinity of KIX for the BODIPY-conjugated pKID domain ($pKID^{BODIPY}$) of the CREB protein using the fluorescence polarization (FP) assay.[17] The results showed that the KIX domains fused to the double-shell system still maintained its function (Figure 1d).

The cryo-EM raw image shows particles with extra densities around apoferritin, indicating the existence of the MKF nanostructure (Figure 2a). Further 2D class averages clearly display three layers, a smeared outer shell MBP, middle cargo protein KIX, and inner shell apoferritin, which is consistent with our design (Figure 1 and Figure 2b). Using single-particle analysis, we determined the three-dimensional (3D) structure of MKF from ∼37,000 particles and achieved an overall resolution of 2.6 Å (Figure 2c,d and Figure S2a and Table S1). The apoferritin and KIX domain are well resolved at 2.2−2.5 and 3.0−4.0 Å, respectively (Figure S2b), confirmed by Q-scores[18] developed for evaluating the density resolvability (Figure 2e). However, the MBP portion cannot be resolved presumably due to the high flexibility of the linker between the MBP and KIX domain. Notably, the KIX domain shows a directional resolution distribution; the closer to the apoferritin inner shell, the higher resolution obtained, demonstrating that the KIX domain closer to apoferritin is more stable. The cysteine mutations on T27 and A31 of KIX distributed between two α-helix domains form disulfide bonds with the cysteine mutations on E169 and E237 of adjacent apoferritin, respectively, may be attributable to the increased stability of the KIX structure as designed (Figure 2f). The resulting MKF shell structure shows that the KIX domain retains the original three helix bundle structures determined by NMR and X-ray crystallography, with RMSD values of 1.26 to 1.59 Å when superimposed with the NMR (1KDX, 2AGH, 2LSX) and X-

https://doi.org/10.1021/acscentsci.1c01090
ACS Cent. Sci. 2022, 8, 214−222

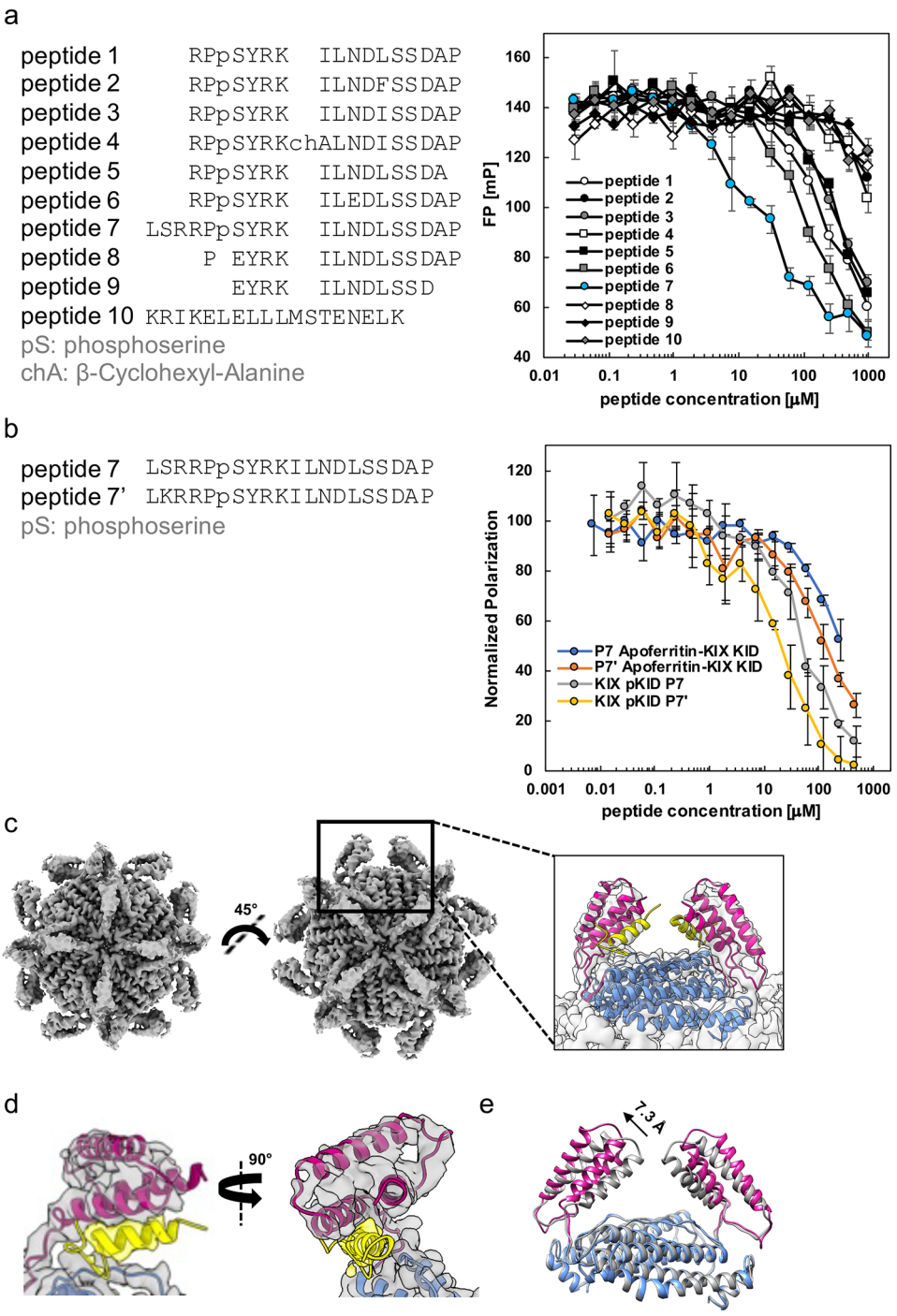

Figure 3. KIX-binding peptide design and the cryo-EM map of peptide bound to MKF. a. List of the designed KIX-binding peptides (left panel). N- and C-termini of the peptides are capped by acetylation and amidation, respectively. Fluorescence polarization assay using the BODIPY-conjugated phosphorylated KID domain of CREB and the KIX domain of CBP with KIX-binding peptides (right panel). The average of fluorescence polarization was plotted with the standard deviation (n = 3). b. Sequence alignment of two peptides 7 and 7′ on the left and FP assay comparisons of these peptides with the KIX domain alone and MBP-KIX-apoferritin. c. Left, the reconstructed cryo-EM map of MKF-peptide-7 in two different views. Right, zoomed view of the extra density after the modeling of the KIX domain. d. Cryo-EM density of single KIX-peptide-7 with model fitted. KIX and peptide 7 are depicted as violet red and gold, respectively; the helical-like density corresponding to peptide 7 is separable and shown with a gold transparent surface. e. Superimposing models of MKF (gray) and MKF-peptide-7 (green) to demonstrate the KIX domain movement. Peptide 7 in MKF-peptide-7 is hidden for better display.

ray structures (4I9O, 5SVH) (Table S2). With the success of the structure determination of MKF, we further investigated whether the double-shell system can be applied to therapeutically relevant binding partners of KIX like those upregulated in AML. The current treatments for AML are mainly chemotherapy or stem cell transplantation, which have strong side effects and are often unsuccessful. Hence, inhibiting the interaction between the pKID domain of CREB and the KIX domain may provide a more specific treatment for this disease, with fewer side effects. Unlike tyrosine kinases, the

https://doi.org/10.1021/acscentsci.1c01090
ACS Cent. Sci. 2022, 8, 214−222

identification of small molecules to disrupt protein−protein interactions have traditionally been difficult due to large and relatively flat surface areas. To this end, we developed a novel approach to target the interaction between CBP and CREB. We used computational approaches to design 10 peptides to mimic pKID and act as competitive inhibitors of the pKID-KIX interaction (see Materials and Methods). We used molecular dynamics simulations to identify minimal segments of pKID, 16−19 amino acid residues in length, that were predicted to maintain key interaction hotspots. We also proposed sequence variations to explore these hotspots, and we capped both N- and C-termini with neutral groups to further stabilize the peptides (Figure 3a). The synthesized peptides were tested using the FP assay with the KIX-pKID^{BODIPY} complex. Among the 10 computationally designed peptides, peptide 7 had the strongest *in vitro* binding affinity to the KIX domain and was selected to form a complex with MKF, hereafter referred to as MKF-peptide-7.

Using a similar single-particle cryo-EM processing strategy on the MKF-peptide-7 complex, we obtained a 3D reconstruction of the complex at an overall resolution of 2.3 Å (Figure 3c, Figures S3, S4, and Table S1). Similar to MKF, the apoferritin and KIX domain are well resolved, while the MBP density is noisy (Figure S4b−d). After modeling with apoferritin and KIX, we found an extra density bound to KIX, which should be derived from peptide 7 (Figure 3c), but we can only resolve its density at ∼4.5 Å (Figure 3d, Figure S4d). Then, we used the particle symmetry expansion and focused classification options in the Relion software package[19] for further image processing, aiming to improve the resolution for a single subunit. However, this strategy failed, possibly due to the disruption of disulfide bonds between one KIX and its neighboring apoferritin subunit. Compared to MKF, the KIX domain in the MKF-peptide-7 complex moves outward by 7.3 Å upon the binding of peptide 7 (Figure 3e), suggesting that our double-shell system allows the movement of the cargo protein (KIX) to provide binding space for its partner (peptide 7) to avoid clashes with apoferritin.

To investigate how these structural observations can be correlated with FP assay results using the MKF scaffold in complex with pKID, we performed comparative FP assays using both the MKF-pKID^{BODIPY} and KIX-pKID^{BODIPY} complexes. Here, we monitored FP signals from pKID^{BODIPY} by adding either peptide 7 or 7′ in a dilution series into solutions of the complexes of KIX (or MKF) and pKID^{BODIPY} (Figure 3b, Figure S6, and Table S3). The inhibition of the MKF-pKID^{BODIPY} interaction (IC_{50} 311 μM) by peptide 7 was 6 times weaker than that of the KIX-pKID^{BODIPY} (IC_{50} 50.0 μM). Since we could not observe full inhibition by peptide 7 due to its solubility at higher than 2 mM, we also used another variant peptide, 7′ with an N-terminal serine to lysine mutation. The new peptide showed a slightly stronger IC_{50} (24.2 μM), i.e., smaller value, compared with KIX alone versus peptide 7 (50.0 μM) and full inhibition at the peptide concentration of 500 μM (Figure 3b). In addition, the IC_{50} value of peptide 7′ against the MKF-pKID^{BODIPY} complex was 170 μM, 7 times that of KIX-pKID^{BODIPY} (24.2 μM). In both cases of peptides 7 and 7′, the MKF scaffold shows 6 to 7 times weaker inhibition, i.e., larger IC_{50} values, compared to the KIX domain only. Together with the functional assay that shows the strong binding affinity of KIX for peptide 7 and 7′, our results indicate that these peptides can be used as initial candidates of KIX-pKID inhibitors for further improvements.

Interestingly, although our designed peptide is a truncated portion of the pKID helix that binds to KIX, we found that the binding mode of peptide 7 to KIX (Figure S5a and Figure S7) differs from that of the corresponding region in pKID (PDB: 1KDX[20]). In the previously published structure, the main α-helix of pKID at the interaction surface contacts two helices α1 and α3 of KIX, known as the cMyb/pKID binding surface,[21] where hydrophobic residues pack into a pocket (Figure S5b and Figure S7). In our structure, peptide 7 instead forms a helix−helix interaction with only a single KIX helix, α3, i.e., the part of the cMyb/pKID binding surface. Comparing the two structures shows that the angle of the helices from the extended pKID domain vs peptide 7 is offset by 30.9° (Figure S5c,d), further confirming the discovery of a unique binding mode of peptide 7 and KIX. This provides opportunities for further optimization with additional stabilization, for example, introducing staples across different parts of the helix. In addition, the orientation of the KIX domain's three helix bundle on the apoferritin shell surface exposes its mixed lineage leukemia (MLL) binding surface[21] toward the exterior of the KIX-apoferritin shell (Figure S7) making it accessible for binding of peptides/compounds, which could be used for developments of the KIX/MLL interaction inhibitors.

CONCLUSIONS

The theoretical atomic resolution limit of 38 kDa for single-particle cryo-EM analysis (SPA) was proposed in 1995.[15] Until now, this limit has not yet been broken, pointing to the approximate truth that SPA is limited to samples below 38 kDa. In this study, we established the double-shell system, which can be applied in determining the structure of proteins as small as 11 kDa at near-atomic resolution, thereby broadening the application range of SPA. The 11 kDa KIX as the cargo protein in this work was resolved at near-atomic resolution, and its 19 residue peptide inhibitor was also detectable, suggesting that our double-shell system can also resolve peptides, which may, in future, assist structure-based drug design. Though our structure does not yet resolve atomic details, the site of interaction between small molecules and the targeted protein is important information to validate our design principle and to encourage the next phase of the drug development pipeline. In addition to interacting with pKID, the KIX domain also interacts with many other human and viral proteins, such as transcription factors p53 and FOXO3a, breast cancer type 1 susceptibility protein (BRCA1), and Tat protein of human immunodeficiency virus type 1 (HIV-1).[22] Therefore, the MKF design in this study can be applied to drug discovery for all these related diseases. Furthermore, to apply the double-shell system in a more universal way, the selected cargo proteins should have a known structure, which allows the iterative design of the disulfide bonds to achieve a stable complex suitable for cryo-EM analysis. Finally, the double-shell system may also play a role in vaccine development; e.g., fusion of the receptor-binding domain (RBD) of the spike protein of SARS-Cov-2 (COVID-19) to apoferritin could make them rigidly displayed on the apoferritin cage to mimic the virus and then be used as a potential vaccine.[23−26]

MATERIALS AND METHODS

No unexpected or unusually high safety hazards were encountered.

https://doi.org/10.1021/acscentsci.1c01090
ACS Cent. Sci. 2022, 8, 214−222

Protein Expression and Purification. The KIX domain (588−672) of CBP and mouse apoferritin were grafted into the pMAL-c5X vector. To stabilize the KIX domain of CBP on apoferritin, five C-terminal amino acids of the KIX domain of CBP and five N-terminal amino acids of apoferritin were truncated from the construct. The site-directed mutagenesis was performed to introduce mutations in MBP-KIX-apoferritin (T27C, A31C, E169C, C177S, and E237C) (Figure S1a). The MBP-KIX-apoferritin constructs were bacterially expressed in BL21 (DE3) and purified using amylose resin (New England Biolabs) with 20 mM maltose. The 24-mer MBP-KIX-apoferritin complex was further purified using HiLoad 16/600 Superdex 200 pg (Cytiva) from incomplete KIX-apoferritin complex and its monomer in 30 mM HEPES-NaOH (pH 7.5) containing 150 mM sodium chloride. Trehalose (final concentration: 5%) was added to the samples. For MBP-KIX-apoferritin in complex with the peptide 7, the purified MBP-KIX-apoferritin was mixed with the peptide 7 and stored at 4 °C.

Computational Design of Therapeutic Peptides. The CREB protein is 340 amino acid residues in length and contains the pKID domain, which is 28 residues in length. To design a short peptide that would compete with pKID, we used molecular dynamics simulations to first study the interface between pKID and KIX to identify hotspot interactions. Hotspots were defined by measuring the highest frequency interactions between KIX and pKID (hydrophobic contacts, hydrogen bonds, salt bridges, and cation−π interactions). We additionally performed simulations of truncated versions of the pKID domain that would maintain these interactions as well as several mutants. Simulation coordinates were prepared from the previously published pKID-KIX NMR structure.[20] Prime was used to model missing side chains, and neutral acetyl and methylamide groups were added to cap the protein termini. PropKa was used to determine the dominant protonation state of all titratable residues at pH 7. Dabble was used to place the protein complex into a water box ($65 \times 65 \times 65$ Å^3) containing sodium and chloride ions at roughly 150 mM.[27] All simulations were run on a single Graphical Processing Unit (GPU) using the Amber18 Compute Unified Device Architecture (CUDA) version of particle-mesh Ewald molecular dynamics (PMEMD). We used the CHARMM36m parameters for proteins, sodium, and chloride ions, and the TIP3P model for waters. Protocols for minimization, equilibration, and production are described in the previous publications.[27,28] All simulations were 1 μs in length. To analyze the stability of the peptide−KIX interaction, we calculated the root-mean-square fluctuation (RMSF) of the peptides after aligning the complex to the helical segments of the KIX domain. Using the calculated stabilities (based on RMSF) from these simulations, we selected the optimal peptide segment and most promising mutants to synthesize and test *in vitro* (Figure 3a).

Fluorescence Polarization Assay. Fluorescence polarization (FP) using the MBP-KIX-apoferritin and the BODIPY-conjugated phosphorylated pKID domain (pKID^{BODIPY}) of CREB was performed as described previously.[20] Briefly, the hexahistidine-tagged KID domain of CREB was bacterially expressed and purified using the TALON superflow (Cytiva). After the His-tag cleavage, the KID domain of CREB was further purified using HiLoad 16/600 Superdex 75 pg (Cytiva). The purified KID domain was enzymatically phosphorylated (pKID) by the catalytic subunit of the cAMP-dependent protein kinase A (PKA) (New England Biolabs). Phosphorylation efficiency of pKID, which was assessed using a SDS-gel containing Phos-tag Acrylamide (FUJIFILM), was almost 100%. pKID was purified using the phosphoprotein enrichment kit (Takara). BODIPY TMR C_5-Maleimide (Thermo Fisher Scientific) was conjugated to the N-terminal cysteine residue of the purified pKID, and the unreacted BODIPY-dye was removed using the PD-10 column (Cytiva) twice. In the FP assay using 25 μL of 200 nM conjugated pKID^{BODIPY} was mixed with 25 μL of dilution series of KIX, MBP-KIX-apoferritin construct 3, and MBP-apoferritin (3.9 pM to 10 μM). The molar concentration of KIX, MBP-KIX-apoferritin construct 3, and MBP-apoferritin was calculated as a monomer. FP was measured 30 min after mixing using INFINITE M1000 PRO (TECAN). The experiment was performed 4 times, and the average was plotted with the standard deviation. The designed peptides were synthesized by Thermo Fisher Scientific. For the inhibition assay using the peptides, 25 μL of 400 nM each KIX and pKID^{BODIPY} was mixed with 25 μL of dilution series of peptides (122 nM to 2 mM). The experiment was performed 3 times, and the average was plotted with the standard deviation. The FP assay of MBP-KIX-apoferritin construct 3 with inhibitory peptides 7 (LSRRPpSYRKILNDLSSDAP) and 7′ (LKRRPpSYRKILNDLSSDAP) was performed in triplicate at room temperature in 20 mM Tris-HCl (pH 8.0 @ 20 °C), 150 mM NaCl, and 0.01% Triton-X100. 25 μL of 200 nM MBP-KIX-apoferritin and pKID^{BODIPY} was incubated for 30 min with inhibitory peptides at a concentration range of 0.008−500 μM in the dark. Fluorescence polarization was then measured using the INFINITE M1000 PRO plate reader.

Cryo-EM Data Acquisition. The samples were diluted at a final concentration of around 0.5 mg/mL for both the MBP-KIX-apoferritin complex (MKF) and MKF-peptide-7 complex. Three microliters of the samples were applied onto glow-discharged 200-mesh R2/1 Quantifoil copper grids coated with continuous carbon. The grids were blotted for 2 s and rapidly cryocooled in liquid ethane using a Vitrobot Mark IV (Thermo Fisher Scientific) at 4 °C and 100% humidity. The samples were screened using a Talos Arctica cryo-electron microscope (Thermo Fisher Scientific) operated at 200 kV. They were then imaged in a Titan Krios cryo-electron microscope (Thermo Fisher Scientific) operated at 300 kV with GIF energy filter (Gatan) at a magnification of 165,000× (corresponding to a calibrated sampling of 0.82 Å per pixel) for both samples. Micrographs were recorded by EPU software (Thermo Fisher Scientific) with a Gatan K2 Summit direct electron detector, where each image was composed of 30 individual frames with an exposure time of 6 s and an exposure rate of 7.3 electrons per second per Å^2. A total of 1915 movie stacks for the MKF and 2490 movie stacks for the MKF-peptide-7 complex were collected.

Single-Particle Image Processing and 3D Reconstruction. All micrographs were first imported into Relion[19] for image processing. The motion correction was performed using MotionCor2[29] and the contrast transfer function (CTF) was determined using CTFFIND4.[30] Then, the micrographs with "rlnMotionEarly < 10" and "rlnCtfMaxResolution < 5" were selected using the "subset selection" option in Relion. All particles were autopicked using the NeuralNet option in EMAN2.[31] Then, particle coordinates were imported to Relion, where the poor 2D class averages were removed by several rounds of 2D classification. The initial models for both

https://doi.org/10.1021/acscentsci.1c01090
ACS Cent. Sci. 2022, 8, 214−222

data sets were built in cryoSPARC[32] using the ab initio reconstruction option with octahedral symmetry applied separately. For the MKF, 167,662 particles were picked and 124,114 were selected after 2D classification in Relion. After removing bad classes by 3D classification, the 3D refinement was performed using 53,550 particles, and a 2.7 Å resolution map was obtained, then heterogeneous refinement was applied in cryoSPARC to further clean up the particle images. Final homogeneous refinement was performed using 37,386 particles, and a 2.57 Å resolution map was obtained. For the MKF-peptide-7, 113,154 particles were picked, and 110,232 were selected after 2D classification in Relion. After removing bad classes by 3D classification, the 3D refinement was performed using 62,100 particles, and a 2.51 Å resolution map was obtained, then heterogeneous refinement was applied in cryoSPARC to further clean up the particle images. Final homogeneous refinement was performed using 35,613 particles, and a 2.3 Å resolution map was obtained. Resolutions for the final maps were estimated using the 0.143 criterion of the Fourier shell correlation (FSC) curve without or with a mask. A Gaussian low-pass filter was applied to the final 3D maps displayed in the UCSF Chimera software package.[33] (See more information in Figures S2, S3, and S4 and Table S1.)

Model Building. Model building was first conducted on the cryo-EM map of the MBP-KIX-Ferritin complex (MKF). The MKF protomer consists of apoferritin and KIX. The crystal structures of apoferritin protomer (PDB ID: 3WNW) and KIX (PDB ID: 4I9O) were rigidly fitted into the cryo-EM map, followed by refinement using phenix.real_space_refine[34] with secondary structure and geometry restraints. Coot[35] was applied to manually optimize the model. The protomer model was then fitted into the cryo-EM density of the other protomers with Chimera,[36] and optimized using phenix.real_space_refine.

As the protomer was conformationally different in the cryo-EM density of the MKF-peptide-7 complex compared with MKF, molecular dynamics flexible fitting (MDFF)[37] was performed on the MKF-peptide-7 protomer using the MKF protomer as the initial model. Each run of MDFF included 10^4 minimization steps and 10^5 molecular dynamics steps, and the MDFF was stopped after no noticeable structural changes. The resultant model was refined using phenix.real_space_refine. The NMR structure of pKID (residues 128−146 corresponding to 1−19 residues of peptide-7) was then rigidly docked into the extra density adjacent to KIX and optimized by Coot and phenix.real_space_refine. The protomer model was then fitted into the cryo-EM density of the other protomers with Chimera, and optimized using phenix.real_space_refine.

The final models were evaluated by MolProbity[38] as previously stated.[39] The agreement between the map and model for each of the residues and the map density resolvability are evaluated by the Q scores.[18] Statistics of the map reconstruction and model building are summarized in Table S1. All figures were prepared using PyMol[40] and Chimera.

■ ASSOCIATED CONTENT

Supporting Information

The Supporting Information is available free of charge at https://pubs.acs.org/doi/10.1021/acscentsci.1c01090.

All designed constructs of the MKF; Workflow of cryo-EM data processing and resolution maps of MKF; Single-particle cryo-EM analysis of the MKF-peptide-7 complex; Map quality and model validation of MKF-peptide-7; Comparison of previously published NMR data to our cryo-EM structure; Fluorescence polarization assay of KIX and MKF in complex with $pKID^{BODIPY}$ by inhibitors; Orientation of the KIX domain on the MFK scaffold; Orientation of the KIX domain on the MFK scaffold; Superposition of the KIX domains of MKF and MKF-peptide-7 with the NMR and X-ray structures; IC_{50} values (PDF)

■ AUTHOR INFORMATION

Corresponding Authors

Kaiming Zhang − *MOE Key Laboratory for Cellular Dynamics and Division of Life Sciences and Medicine, University of Science and Technology of China, Hefei 230027, China; Department of Bioengineering, Stanford University, Stanford, California 94305, United States;* orcid.org/0000-0003-0414-4776; Email: kmzhang@ustc.edu.cn

Wah Chiu − *Department of Bioengineering, Stanford University, Stanford, California 94305, United States; CryoEM and Bioimaging Division, Stanford Synchrotron Radiation Lightsource, SLAC National Accelerator Laboratory, Stanford University, Menlo Park, California 94025, United States;* orcid.org/0000-0002-8910-3078; Email: wahc@stanford.edu

Soichi Wakatsuki − *Department of Structural Biology, Stanford University, Stanford, California 94305, United States; Biosciences Division, SLAC National Accelerator Laboratory, Stanford University, Menlo Park, California 94025, United States;* orcid.org/0000-0001-5896-7968; Email: soichi.wakatsuki@stanford.edu

Kathleen M. Sakamoto − *Department of Pediatrics, Stanford University School of Medicine, Stanford, California 94305, United States;* Email: kmsakamo@stanford.edu

Authors

Naoki Horikoshi − *Life Science Center for Survival Dynamics, University of Tsukuba, Tsukuba, Ibaraki 305-8577, Japan; Department of Structural Biology, Stanford University, Stanford, California 94305, United States*

Shanshan Li − *MOE Key Laboratory for Cellular Dynamics and Division of Life Sciences and Medicine, University of Science and Technology of China, Hefei 230027, China; Department of Bioengineering, Stanford University, Stanford, California 94305, United States*

Alexander S. Powers − *Department of Chemistry and Department of Computer Science, Stanford University, Stanford, California 94305, United States*

Mikhail A. Hameedi − *Department of Structural Biology, Stanford University, Stanford, California 94305, United States; Biosciences Division, SLAC National Accelerator Laboratory, Stanford University, Menlo Park, California 94025, United States*

Grigore D. Pintilie − *Department of Bioengineering, Stanford University, Stanford, California 94305, United States*

Hee-Don Chae − *Department of Pediatrics, Stanford University School of Medicine, Stanford, California 94305, United States*

Yousuf A. Khan − *Department of Computer Science, Stanford University, Stanford, California 94305, United States; Department of Molecular and Cellular Physiology, Stanford*

https://doi.org/10.1021/acscentsci.1c01090
ACS Cent. Sci. 2022, 8, 214−222

University School of Medicine, Stanford, California 94305, United States; orcid.org/0000-0003-0201-2796

Carl-Mikael Suomivuori − *Department of Computer Science, Stanford University, Stanford, California 94305, United States*

Ron O. Dror − *Department of Computer Science, Stanford University, Stanford, California 94305, United States;* orcid.org/0000-0002-6418-2793

Complete contact information is available at: https://pubs.acs.org/10.1021/acscentsci.1c01090

Author Contributions

#K.Z. and N.H. contributed equally to this work. K.Z. and S.W. conceived the study. K.Z., N.H., W.C., and S.W. designed experiments. N.H. and M.A.H. prepared the samples and performed the functional assay. K.Z. performed cryo-EM sample preparation, screening, data collection, image processing, and structure determination. N.H. and S.L. assisted with the cryo-EM screening and data collection. A.S.P. and C.-M.S. designed the peptides, with input from H.C., N.H., and S.W. S.L. and K.Z. built the models. K.Z., N.H., S.L., G.D.P., A.S.P., M.A.H., C.-M.S., Y.A.K., R.O.D., K.S., W.C., and S.W. analyzed data; and K.Z., S.L., N.H., S.W., and W.C. wrote the manuscript with input from other authors.

Notes

The authors declare no competing financial interest.

Data Availability: Cryo-EM maps of the MBP-KIX-apoferritin complex (MKF) and MKF-peptide-7 complex with their associated atomic models have been deposited in the Electron Microscopy Data Bank and the Protein Data Bank under accession codes 7TB3 and EMD-25791, and PDB ID codes 7TBH and EMD-25799, respectively.

■ ACKNOWLEDGMENTS

We thank Martin Vögele and Siri van Keulen for helpful suggestions and insights. We also thank the facilities at Stanford-SLAC and USTC Cryo-EM Center. This work was supported by the National Institutes of Health grants (P41GM103832, R01GM079429, and S10OD021600 to W.C.). Pediatric Cancer Research Foundation, Stanford Maternal Child Health Research Institute (K.M.S., S.W., R.O.D.). Stanford Clinical and Translational Innovation grant, Stanford SPARK program, and Leukemia and Lymphoma Society (K.M.S.). The National Natural Science Foundation of China 31621002 and 91854203 (X.Y.) and start-up funding by the University of Science and Technology of China KY9100000032 and KJ2070000080 (K.Z.).

■ REFERENCES

(1) Herzik, M. A., Jr; Wu, M.; Lander, G. C. High-Resolution Structure Determination of Sub-100 kDa Complexes Using Conventional Cryo-EM. *Nat. Commun.* **2019**, *10* (1), 1032.

(2) Khoshouei, M.; Radjainia, M.; Baumeister, W.; Danev, R. Cryo-EM Structure of Haemoglobin at 3.2 Å Determined with the Volta Phase Plate. *Nat. Commun.* **2017**, *8*, 16099.

(3) Fan, X.; Wang, J.; Zhang, X.; Yang, Z.; Zhang, J.-C.; Zhao, L.; Peng, H.-L.; Lei, J.; Wang, H.-W. Single Particle Cryo-EM Reconstruction of 52 kDa Streptavidin at 3.2 Angstrom Resolution. *Nat. Commun.* **2019**, *10* (1), 2386.

(4) Liu, Y.; Gonen, S.; Gonen, T.; Yeates, T. O. Near-Atomic Cryo-EM Imaging of a Small Protein Displayed on a Designed Scaffolding System. *Proc. Natl. Acad. Sci. U. S. A.* **2018**, *115* (13), 3362−3367.

(5) Liu, Y.; Huynh, D. T.; Yeates, T. O. A 3.8 Å Resolution Cryo-EM Structure of a Small Protein Bound to an Imaging Scaffold. *Nat. Commun.* **2019**, 1 DOI: 10.1038/s41467-019-09836-0.

(6) Coscia, F.; Estrozi, L. F.; Hans, F.; Malet, H.; Noirclerc-Savoye, M.; Schoehn, G.; Petosa, C. Fusion to a Homo-Oligomeric Scaffold Allows Cryo-EM Analysis of a Small Protein. *Sci. Rep.* **2016**, *6*, 30909.

(7) Yao, Q.; Weaver, S. J.; Mock, J.-Y.; Jensen, G. J. Fusion of DARPin to Aldolase Enables Visualization of Small Protein by cryoEM. *Structure* **2019**, *27*, 1148.

(8) Zhang, K.; Li, S.; Kappel, K.; Pintilie, G.; Su, Z.; Mou, T.-C.; Schmid, M. F.; Das, R.; Chiu, W. Cryo-EM Structure of a 40 kDa SAM-IV Riboswitch RNA at 3.7 Å Resolution. *Nat. Commun.* **2019**, *10* (1), 5511.

(9) Shankar, D. B.; Cheng, J. C.; Kinjo, K.; Federman, N.; Moore, T. B.; Gill, A.; Rao, N. P.; Landaw, E. M.; Sakamoto, K. M. The Role of CREB as a Proto-Oncogene in Hematopoiesis and in Acute Myeloid Leukemia. *Cancer Cell* **2005**, *7* (4), 351−362.

(10) Mitton, B.; Chae, H.-D.; Hsu, K.; Dutta, R.; Aldana-Masangkay, G.; Ferrari, R.; Davis, K.; Tiu, B. C.; Kaul, A.; Lacayo, N.; Dahl, G.; Xie, F.; Li, B. X.; Breese, M. R.; Landaw, E. M.; Nolan, G.; Pellegrini, M.; Romanov, S.; Xiao, X.; Sakamoto, K. M. Small Molecule Inhibition of cAMP Response Element Binding Protein in Human Acute Myeloid Leukemia Cells. *Leukemia* **2016**, *30* (12), 2302−2311.

(11) Denis, C. M.; Chitayat, S.; Plevin, M. J.; Wang, F.; Thompson, P.; Liu, S.; Spencer, H. L.; Ikura, M.; LeBrun, D. P.; Smith, S. P. Structural Basis of CBP/p300 Recruitment in Leukemia Induction by E2A-PBX1. *Blood* **2012**, *120* (19), 3968−3977.

(12) Zhang, K.; Pintilie, G. D.; Li, S.; Schmid, M. F.; Chiu, W. Resolving Individual Atoms of Protein Complex by Cryo-Electron Microscopy. *Cell Res.* **2020**, *30* (12), 1136−1139.

(13) Brüschweiler, S.; Konrat, R.; Tollinger, M. Allosteric Communication in the KIX Domain Proceeds through Dynamic Repacking of the Hydrophobic Core. *ACS Chem. Biol.* **2013**, *8* (7), 1600−1610.

(14) Wang, N.; Majmudar, C. Y.; Pomerantz, W. C.; Gagnon, J. K.; Sadowsky, J. D.; Meagher, J. L.; Johnson, T. K.; Stuckey, J. A.; Brooks, C. L.; Wells, J. A.; Mapp, A. K. Ordering a Dynamic Protein Via a Small-Molecule Stabilizer. *J. Am. Chem. Soc.* **2013**, *135*, 3363−3366.

(15) Henderson, R. The Potential and Limitations of Neutrons, Electrons and X-Rays for Atomic Resolution Microscopy of Unstained Biological Molecules. *Q. Rev. Biophys.* **1995**, *28* (2), 171−193.

(16) Radhakrishnan, I.; Pérez-Alvarado, G. C.; Parker, D.; Dyson, H. J.; Montminy, M. R.; Wright, P. E. Structural Analyses of CREB-CBP Transcriptional Activator-Coactivator Complexes by NMR Spectroscopy: Implications for Mapping the Boundaries of Structural Domains. *J. Mol. Biol.* **1999**, *287* (5), 859−865.

(17) Chae, H.-D.; Cox, N.; Capolicchio, S.; Lee, J. W.; Horikoshi, N.; Kam, S.; Ng, A. A.; Edwards, J.; Butler, T.-L.; Chan, J.; Lee, Y.; Potter, G.; Capece, M. C.; Liu, C. W.; Wakatsuki, S.; Smith, M.; Sakamoto, K. M. SAR Optimization Studies on Modified Salicylamides as a Potential Treatment for Acute Myeloid Leukemia through Inhibition of the CREB Pathway. *Bioorg. Med. Chem. Lett.* **2019**, *29* (16), 2307−2315.

(18) Pintilie, G.; Zhang, K.; Su, Z.; Li, S.; Schmid, M. F.; Chiu, W. Measurement of Atom Resolvability in Cryo-EM Maps with Q-Scores. *Nat. Methods* **2020**, *17* (3), 328−334.

(19) Scheres, S. H. W. RELION: Implementation of a Bayesian Approach to Cryo-EM Structure Determination. *J. Struct. Biol.* **2012**, *180* (3), 519−530.

(20) Radhakrishnan, I.; Pérez-Alvarado, G. C.; Parker, D.; Dyson, H. J.; Montminy, M. R.; Wright, P. E. Solution Structure of the KIX Domain of CBP Bound to the Transactivation Domain of CREB: A Model for Activator:coactivator Interactions. *Cell* **1997**, *91* (6), 741−752.

(21) De Guzman, R. N.; Goto, N. K.; Dyson, H. J.; Wright, P. E. Structural Basis for Cooperative Transcription Factor Binding to the CBP Coactivator. *J. Mol. Biol.* **2006**, *355* (5), 1005−1013.

(22) Thakur, J. K.; Yadav, A.; Yadav, G. Molecular Recognition by the KIX Domain and Its Role in Gene Regulation. *Nucleic Acids Res.* **2014**, *42* (4), 2112−2125.
(23) Bianchi, M.; Turner, H. L.; Nogal, B.; Cottrell, C. A.; Oyen, D.; Pauthner, M.; Bastidas, R.; Nedellec, R.; McCoy, L. E.; Wilson, I. A.; Burton, D. R.; Ward, A. B.; Hangartner, L. Electron-Microscopy-Based Epitope Mapping Defines Specificities of Polyclonal Antibodies Elicited during HIV-1 BG505 Envelope Trimer Immunization. *Immunity* **2018**, *49* (2), 288−300.
(24) Al-Halifa, S.; Gauthier, L.; Arpin, D.; Bourgault, S.; Archambault, D. Nanoparticle-Based Vaccines Against Respiratory Viruses. *Front. Immunol.* **2019**, *10*, 22.
(25) Reljic, R.; González-Fernández, Á. Editorial: Nanoparticle Vaccines Against Infectious Diseases. *Front. Immunol.* **2019**, *10*, 2615.
(26) Wang, Z.; Gao, H.; Zhang, Y.; Liu, G.; Niu, G.; Chen, X. Functional Ferritin Nanoparticles for Biomedical Applications. *Front Chem. Sci. Eng.* **2017**, *11* (4), 633−646.
(27) Sicilia, M.-A.; García-Barriocanal, E.; Sánchez-Alonso, S. Community Curation in Open Dataset Repositories: Insights from Zenodo. *Procedia Computer Science* **2017**, *106*, 54−60.
(28) Latorraca, N. R.; Wang, J. K.; Bauer, B.; Townshend, R. J. L.; Hollingsworth, S. A.; Olivieri, J. E.; Xu, H. E.; Sommer, M. E.; Dror, R. O. Molecular Mechanism of GPCR-Mediated Arrestin Activation. *Nature* **2018**, *557* (7705), 452−456.
(29) Zheng, S. Q.; Palovcak, E.; Armache, J.-P.; Verba, K. A.; Cheng, Y.; Agard, D. A. MotionCor2: Anisotropic Correction of Beam-Induced Motion for Improved Cryo-Electron Microscopy. *Nat. Methods* **2017**, *14* (4), 331−332.
(30) Rohou, A.; Grigorieff, N. CTFFIND4: Fast and Accurate Defocus Estimation from Electron Micrographs. *J. Struct. Biol.* **2015**, *192* (2), 216−221.
(31) Tang, G.; Peng, L.; Baldwin, P. R.; Mann, D. S.; Jiang, W.; Rees, I.; Ludtke, S. J. EMAN2: An Extensible Image Processing Suite for Electron Microscopy. *J. Struct. Biol.* **2007**, *157* (1), 38−46.
(32) Punjani, A.; Rubinstein, J. L.; Fleet, D. J.; Brubaker, M. A. cryoSPARC: Algorithms for Rapid Unsupervised Cryo-EM Structure Determination. *Nat. Methods* **2017**, *14* (3), 290−296.
(33) Pettersen, E. F.; Goddard, T. D.; Huang, C. C.; Couch, G. S.; Greenblatt, D. M.; Meng, E. C.; Ferrin, T. E. UCSF Chimera–a Visualization System for Exploratory Research and Analysis. *J. Comput. Chem.* **2004**, *25* (13), 1605−1612.
(34) Adams, P. D.; Afonine, P. V.; Bunkóczi, G.; Chen, V. B.; Davis, I. W.; Echols, N.; Headd, J. J.; Hung, L.-W.; Kapral, G. J.; Grosse-Kunstleve, R. W.; McCoy, A. J.; Moriarty, N. W.; Oeffner, R.; Read, R. J.; Richardson, D. C.; Richardson, J. S.; Terwilliger, T. C.; Zwart, P. H. PHENIX: A Comprehensive Python-Based System for Macromolecular Structure Solution. *In International Tables for Crystallography* **2012**, *F*, 539−547.
(35) Emsley, P.; Lohkamp, B.; Scott, W. G.; Cowtan, K. Features and Development of Coot. *Acta Crystallogr. D Biol. Crystallogr.* **2010**, *66*, 486−501.
(36) Pettersen, E. F.; Goddard, T. D.; Huang, C. C.; Couch, G. S.; Greenblatt, D. M.; Meng, E. C.; Ferrin, T. E. UCSF Chimera–a Visualization System for Exploratory Research and Analysis. *J. Comput. Chem.* **2004**, *25* (13), 1605−1612.
(37) Trabuco, L. G.; Villa, E.; Mitra, K.; Frank, J.; Schulten, K. Flexible Fitting of Atomic Structures into Electron Microscopy Maps Using Molecular Dynamics. *Structure* **2008**, *16* (5), 673−683.
(38) Chen, V. B.; Arendall, W. B., 3rd; Headd, J. J.; Keedy, D. A.; Immormino, R. M.; Kapral, G. J.; Murray, L. W.; Richardson, J. S.; Richardson, D. C. MolProbity: All-Atom Structure Validation for Macromolecular Crystallography. *Acta Crystallogr. D Biol. Crystallogr.* **2010**, *66*, 12−21.
(39) Zhang, K.; Wang, S.; Li, S.; Zhu, Y.; Pintilie, G. D.; Mou, T.-C.; Schmid, M. F.; Huang, Z.; Chiu, W. Inhibition Mechanisms of AcrF9, AcrF8, and AcrF6 against Type I-F CRISPR−Cas Complex Revealed by Cryo-EM. *Proc. Natl. Acad. Sci. U. S. A.* **2020**, *117*, 7176−7182.
(40) Rigsby, R. E.; Parker, A. B. Using the PyMOL Application to Reinforce Visual Understanding of Protein Structure. *Biochem. Mol. Biol. Educ.* **2016**, *44* (5), 433−437.

https://doi.org/10.1021/acscentsci.1c01090
ACS Cent. Sci. 2022, 8, 214−222